

4.2.4.4 Stress Field Determination

With the photoelasticity and CGS analysis complete, the in-plane stress tensor may be determined. Figure 4.30 shows the experimental and theoretical sum and difference of principal stress fields. The $\sigma_1 - \sigma_2$ field is calculated from δ using the Stress-Optic Law in Equation (3.1); the experimental $\sigma_1 - \sigma_2$ compares to the theoretical field just as the δ field compared. The constant of integration c_i is determined from the boundary condition of $\sigma_{\theta\theta} = 0$ along $\theta = \pm\pi$, which requires α , $\sigma_1 - \sigma_2$, and $\sigma_1 + \sigma_2 + c_i$ to calculate. In this case, the crack front has been masked to prevent unwrapping errors across the crack plane; since the horizontal shearing direction data appears to spread the crack region, the actual location of the crack front is under the mask. Therefore a pixel very close to the crack, but a long distance from the crack tip away from error sources, just to the side of the masked region, is chosen as the the location to apply the boundary condition. Here $\sigma_{\theta\theta}$ is taken to be zero at $(r, \theta) = (2.06 \text{ mm}, -3.08 \text{ rad.})$. The resulting experimental $\sigma_1 + \sigma_2$ in Figure 4.30(c) matches the shape of the theoretical field, but does not quite reach as low in value along the crack or as high in front of the crack tip. These errors are most likely due to the smaller experimental x and y derivatives of $\sigma_1 + \sigma_2$ near the crack tip as compared to the theoretical derivatives and due to the slightly smaller x derivative and larger y derivative along the crack.

In Figure 4.31, the experimental and theoretical separated principal stresses are comparable with the same double lobe feature in σ_1 that indents towards the crack tip near $\theta = 0$ and similar flame-like structure emanating for the crack tip in σ_2 . The experimental σ_1 does not indent quite as much as the theoretical case, the experimental σ_2 is not quite as sharp along near $\theta = 0$, and both experimental fields have slightly different behavior approaching the crack behind the tip, but the general structures are similar. These slight differences are due to the errors in those regions from the isoclinic angle, the isochromatic phase, and the CGS phase data as discussed previously. From the isoclinic angle and the principal stresses, the Cartesian stresses in Figure 4.32 are determined. Though the experimental Cartesian stresses have some slight differences from the theoretical fields near the crack tip, due to the error from interpolated points in the isoclinic angle, the experimental fields have similar shape and values as the theoretical. The polar stresses in Figure 4.33 have the

same error locations as the Cartesian stresses due to the isoclinic angle errors, but the experimental polar fields again compare well with the theoretical fields a short distance from the crack tip. The errors ahead and to the side of the crack tip in σ_{rr} and $\sigma_{\theta\theta}$ are along the line of the wrapped isoclinic angle in Figure 4.17(a) corresponding to the false discontinuities that are removed by interpolation. The errors just behind the crack tip in $\sigma_{r\theta}$ are from the isoclinic angle regions that falsely swept through zero in Figure 4.17(a).

These errors propagated from the isoclinic angle demonstrate that the manual corrections to the wrapped field are not perfect, but the generally good comparison of the stress fields demonstrates that these manual corrections are close. New algorithms for correcting for errors in the isoclinic angle data require development; currently, these and other related issues with the isoclinic angle are the last hurdle in phase-shifting photoelasticity (Ramesh, 2009). Each individual user of phase-shifting photoelasticity must determine methods to correct for isoclinic angle errors based on the error sources of their system.

Despite the errors discussed above, the global agreement of the experimental and theoretical fields is excellent, as seen in Table 4.1, which reports the root mean squared deviation (RMS) and the normalized RMS. The low NRMSD values range from 0.012 to 0.051. The lower errors are generally for the fields directly related to the experimental phases such as the derivatives of $\sigma_1 + \sigma_2$, α , and $\sigma_1 - \sigma_2$, with the higher errors in stress fields from combining different fields, like the Cartesian and polar stresses. These higher errors are due to accumulation of errors locally around the crack tip and along the x axis.

A measure of the comparison of the experimental data with the theoretical fracture model is to consider σ_{yy} behavior versus r along the crack plane, since $\sigma_{yy} = K_I/(2\pi r)$ for $\theta = 0$. Figure 4.34 shows the experimental and theoretical σ_{yy} versus r plot and the $\log(\sigma_{yy})$ versus $\log(r)$ plot for $\theta = 0$. The experimental σ_{yy} is slightly smaller than the theoretical, implying a smaller K_I value of $0.442 \text{ MPa}\sqrt{\text{m}}$ on average, but this is most likely due to the errors in the isoclinic angle near $\theta = 0$. The theoretical values fall around the upper error bar, which is $\sigma_{yy} + \text{RMSD}_{\sigma_{yy}}$, showing that this difference along $\theta = 0$ is around the global difference. Despite the smaller absolute values,

the experimental σ_{yy} has the correct $r^{-1/2}$ behavior, evident in the nearly uniform $-1/2$ slope of the experimental $\log(\sigma_{yy})$ versus $\log(r)$ plot in Figure 4.34(b). This $-1/2$ slope also implies that most of the field of view, excluding the masked regions, is in a K_I -dominant region (Anderson, 2005).

Given the K_I dominance for this field of view for this load condition, the error analysis in Section 4.2.4.3 is applicable to the CGS data. Figure 4.35 shows line plots of the experimental $\partial(\sigma_1 + \sigma_2)/\partial x_i$ with \pm RMSD lines and the theoretical $\partial(\sigma_1 + \sigma_2)/\partial x_i$ along the y axis. These plots also indicate the theoretical error ϵ regions given by Equation (4.7) for the CGS approximation of the derivatives of the principal stress sum. For the x derivative from the vertical shearing direction in Figure 4.35(a), the experimental and the theoretical values agree well for $y > \pm 1$ mm, with the theoretical values within the \pm RMSD bounds. The differences between the experimental and theoretical x derivative grow as $|y| \rightarrow 0$, as expected from the $\epsilon > 1\%$ and $\epsilon > 5\%$ error regions. For the y derivative from the horizontal shearing direction in Figure 4.35(b), the experimental and theoretical values compare well for almost all of y , except in the $\epsilon > 5\%$ region for $-y$, with the theoretical values within the RMSD bounds. In comparing the two shearing directions, the vertical shearing data has more error than the horizontal shearing data, indicated by more of y being in the $\epsilon > 1\%$ and $\epsilon > 5\%$ regions, the RMSD being larger, and a larger difference from the theoretical near the crack tip. The general trend of higher error in the vertical shearing data as compared to the horizontal shearing data is true here for this line data and globally as described in Section 4.2.4.3. Error along the crack plane from the vertical shearing direction may explain the slightly higher error in the stress fields directly behind the crack. Despite these errors near the crack, the behavior a short distance from the crack are reasonable, and lead to good global comparison of experimental and theoretical stresses.

Another measure of the comparison of the experimental and theoretical data is the calculated average values for K_I and K_{II} . Theoretical data based on poor K_I and K_{II} values would not compare well globally with experimental data, especially data from two separate experimental methods. The excellent comparison of all the experimental data, spanning two experimental methods, and the theoretical data from the calculated K_I and K_{II} values validates the use of these hybrid experimental methods to investigate stresses near cracks in photoelastic materials.

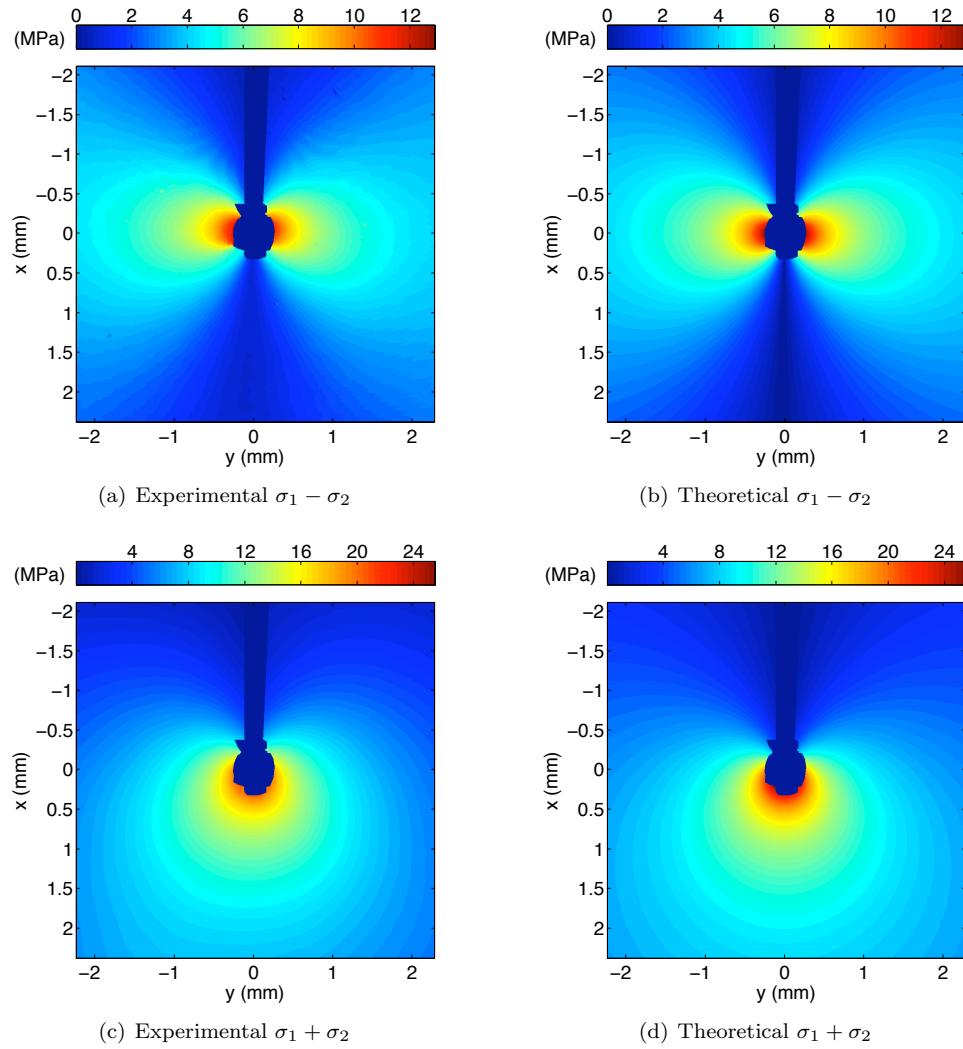


Figure 4.30: Experimental and theoretical data for $\sigma_1 - \sigma_2$ and $\sigma_1 + \sigma_2$ for specimen HomC1 for $K_I = 0.514 \text{ MPa}\sqrt{\text{m}}$ and $K_{II} = 4.4 \text{ kPa}\sqrt{\text{m}}$ with crack region masked in blue

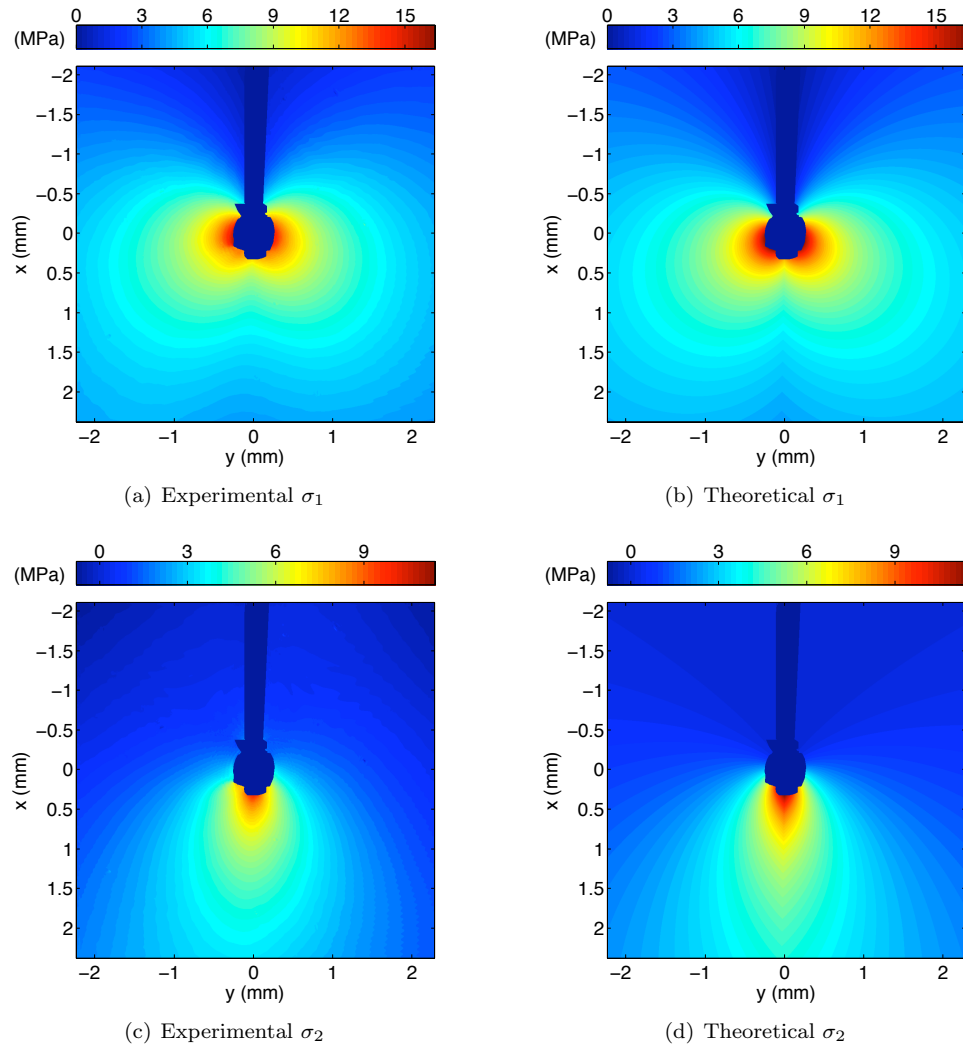


Figure 4.31: Experimental and theoretical data for the principal stresses for specimen HomC1 for $K_I = 0.514 \text{ MPa}\sqrt{\text{m}}$ and $K_{II} = 4.4 \text{ kPa}\sqrt{\text{m}}$ with crack region masked in blue

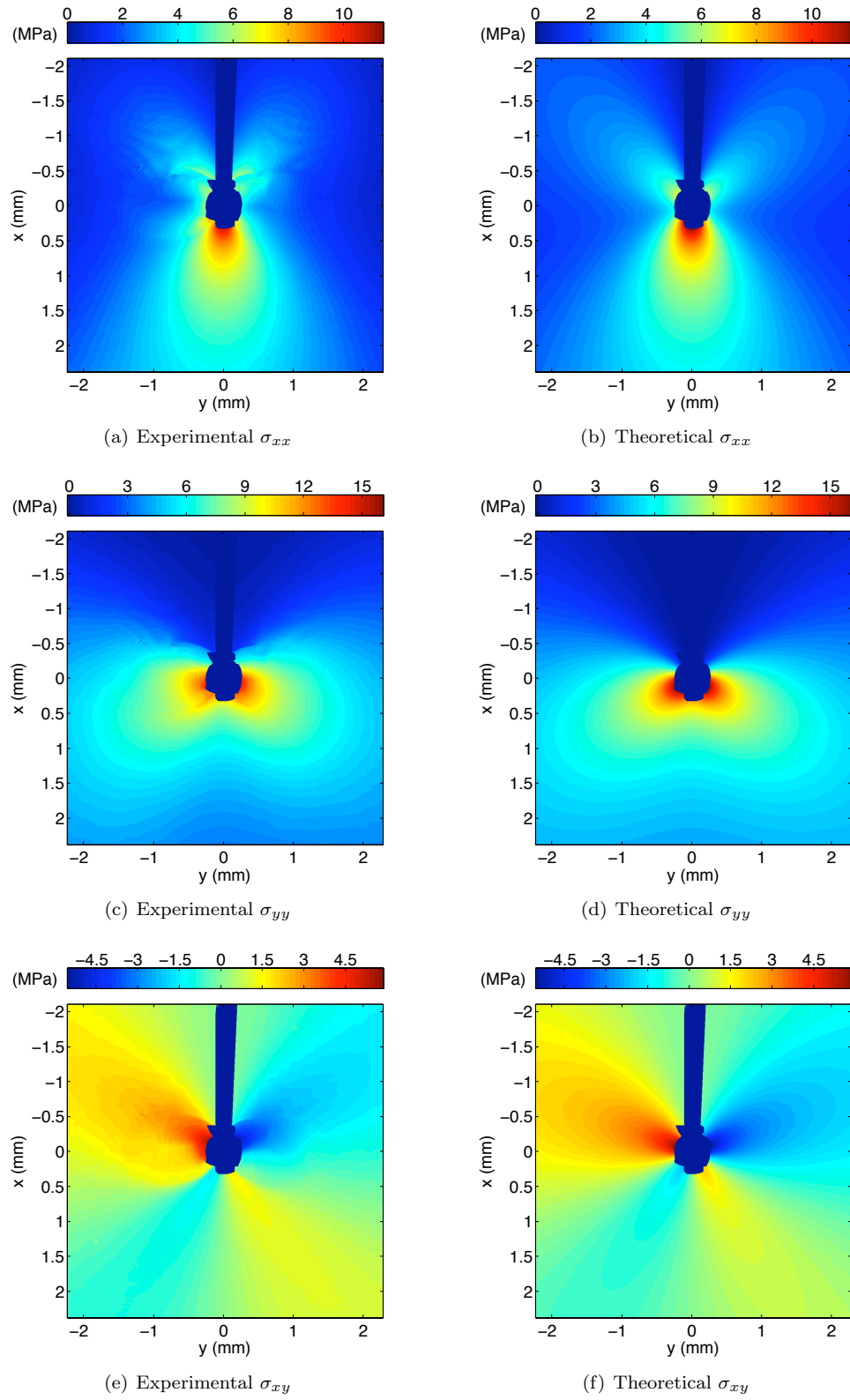


Figure 4.32: Experimental and theoretical data for the Cartesian stresses for specimen HomC1 for $K_I = 0.514 \text{ MPa}\sqrt{\text{m}}$ and $K_{II} = 4.4 \text{ kPa}\sqrt{\text{m}}$ with crack region masked in blue

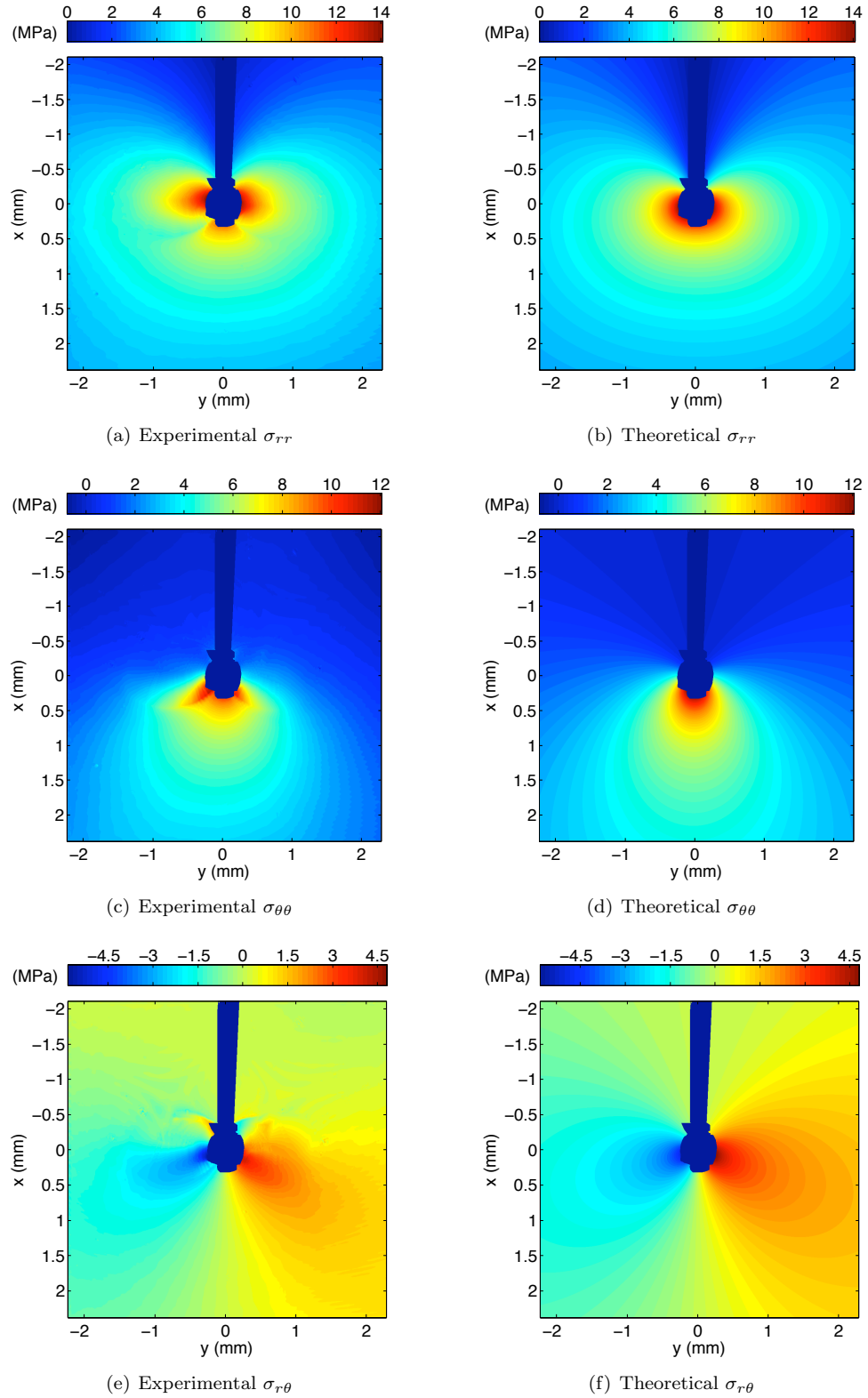


Figure 4.33: Experimental and theoretical data for the polar stresses for specimen HomC1 for $K_I = 0.514 \text{ MPa}\sqrt{\text{m}}$ and $K_{II} = 4.4 \text{ kPa}\sqrt{\text{m}}$ with crack region masked in blue

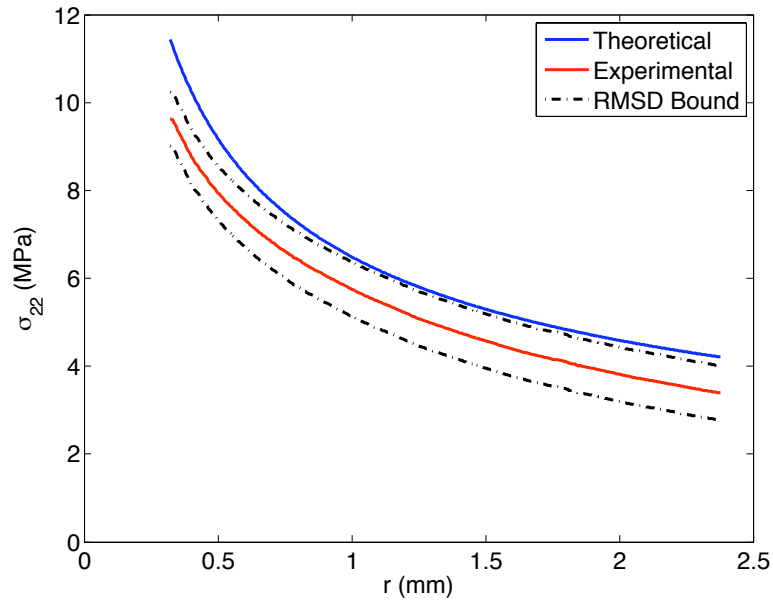
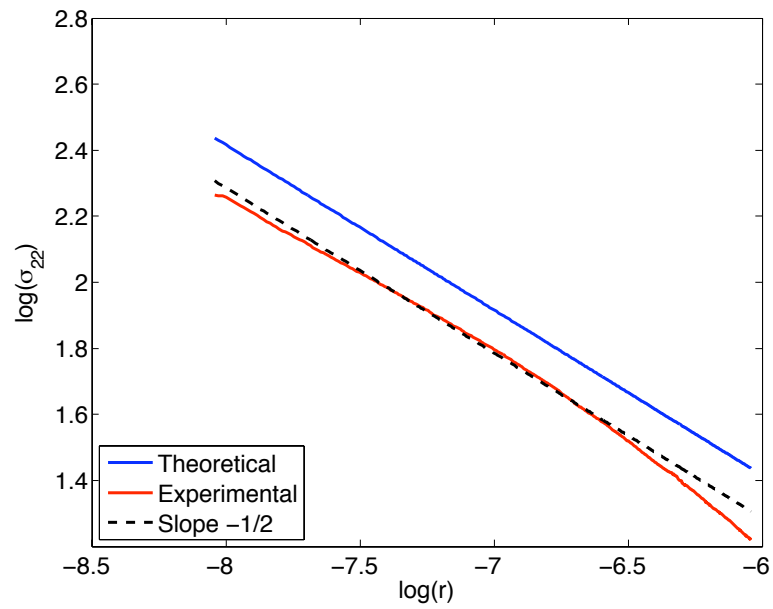
(a) σ_{yy} vs. r for $\theta = 0$ (b) $\log(\sigma_{yy})$ vs. $\log(r)$ for $\theta = 0$

Figure 4.34: Experimental and theoretical data for σ_{yy} along $\theta = 0$ for specimen HomC1 for $K_I = 0.514 \text{ MPa}\sqrt{\text{m}}$ and $K_{II} = 4.4 \text{ kPa}\sqrt{\text{m}}$: The experimental data is slightly lower than the theoretical data, but with similar $r^{-1/2}$ dependence seen by the near $-1/2$ slope on the log-log plot of σ_{yy} versus r .

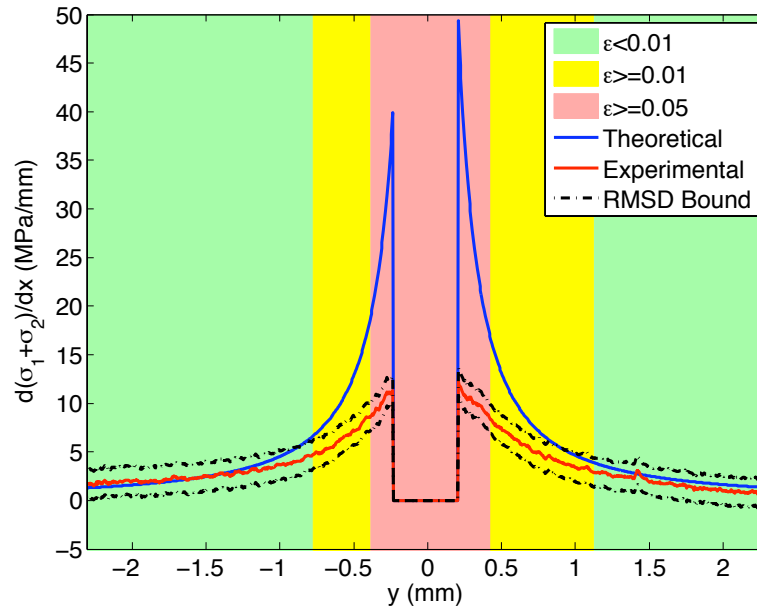
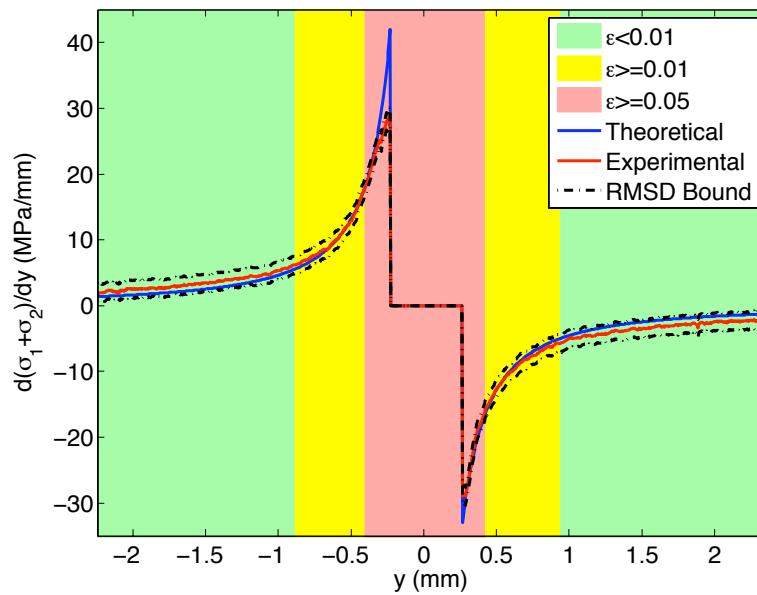
(a) $\frac{\partial(\sigma_1+\sigma_2)}{\partial x}$ vs. y for $\theta = \pm\pi$ (b) $\frac{\partial(\sigma_1+\sigma_2)}{\partial y}$ vs. y for $\theta = \pm\pi$

Figure 4.35: Experimental and theoretical data for $\partial(\sigma_1 + \sigma_2)/\partial x_i$ vs. y for $\theta = \pm\theta$ for specimen HomC1 for $K_I = 0.514 \text{ MPa}\sqrt{\text{m}}$ and $K_{II} = 4.4 \text{ kPa}\sqrt{\text{m}}$: The \pm RMSD error lines and the CGS derivative-approximation error ϵ regions are indicated; the region near the crack tip is masked to zero.

Quantity	Units	RMSD (in Units)	Data Range (in Units)	NRMSD (No Units)
α	rad.	0.17	7.33	0.023
$\varphi_{\alpha d}^{vertical}$	rad.	0.21	4.10	0.051
$\varphi_{\alpha d}^{horizontal}$	rad.	0.06	5.11	0.012
$\partial(\sigma_1 + \sigma_2)/\partial x$ from pure E_x and E_y	MPa/mm	1.53	87.8	0.017
$\partial(\sigma_1 + \sigma_2)/\partial y$ from pure E_x and E_y	MPa/mm	1.30	63.3	0.021
$\partial(\sigma_1 + \sigma_2)/\partial x$ from $\lambda/4$ plate method	MPa/mm	1.47	80.8	0.019
$\partial(\sigma_1 + \sigma_2)/\partial y$ from $\lambda/4$ plate method	MPa/mm	1.33	64.2	0.021
$\sigma_1 + \sigma_2$	MPa	0.60	20.1	0.030
$\sigma_1 - \sigma_2$	MPa	0.25	12.3	0.020
σ_1	MPa	0.36	15.4	0.023
σ_2	MPa	0.29	10.4	0.028
σ_{xx}	MPa	0.48	10.5	0.046
σ_{yy}	MPa	0.62	14.4	0.043
σ_{xy}	MPa	0.30	10.7	0.028
σ_{rr}	MPa	0.42	14.1	0.030
$\sigma_{\theta\theta}$	MPa	0.44	11.8	0.037
$\sigma_{r\theta}$	MPa	0.44	9.0	0.049

Table 4.1: Error analysis for various experimental fields for specimen HomC1 for $K_I = 0.514 \text{ MPa}\sqrt{\text{m}}$ and $K_{II} = 4.4 \text{ kPa}\sqrt{\text{m}}$

4.2.5 Crack with $K_I = 0.259 \text{ MPa}\sqrt{\text{m}}$ and $K_{II} = 5.0 \text{ kPa}\sqrt{\text{m}}$

At a smaller displacement of the wedge that opens the crack in specimen HomC1, the load on the crack causes a stress field with stress intensity factors of $K_I = 0.259 \text{ MPa}\sqrt{\text{m}}$ and $K_{II} = 5.0 \text{ kPa}\sqrt{\text{m}}$. This load is smaller in magnitude than the case presented above, but has a larger mode-mixity with stress intensity factor ratio $\mu_{SIF} = K_{II}/K_I = 0.020$ than the previous case with $\mu_{SIF} = 0.0085$, leading to more asymmetry about the crack plane in the higher mode-mixity case. The experimental parameters are the same for this load case as in the case presented above.

As discussed in the previous case in Section 4.2.4.3, the circularly polarized electric field input for CGS is sufficient for determining the derivatives of $\sigma_1 + \sigma_2$, with similar NRMSD errors presented in Table 4.1 as the pure $E_x \hat{i}$ and $E_y \hat{j}$ method for determining φ_{sum} . The data presented here and